

Article

Preparation of g-C₃N₄/TCNQ Composite and Photocatalytic Degradation of Pefloxacin

Qiuping Li [†], Nuan Wen [†], Wu Zhang, Liansheng Yu, Jinghui Shen, Shuxian Li ^{*} and Yuguang Lv ^{*}

College of Pharmacy, Jiamusi University, Jiamusi 154007, China

^{*} Correspondence: lsxls777@163.com (S.L.); lvyuguang@jmsu.edu.cn (Y.L.)[†] These authors contributed equally to this work.

Abstract: g-C₃N₄ and g-C₃N₄/TCNQ composites with different doping levels were prepared using the copolymerization thermal method with melamine as a precursor. XRD, FT-IR, SEM, TEM, DRS, PL, and I-T characterized them. The composites were successfully prepared in this study. The photocatalytic degradation of pefloxacin (PEF), enrofloxacin (ciprofloxacin), and ciprofloxacin (ciprofloxacin) under visible light ($\lambda > 550$ nm) showed that the composite material had the best degradation effect on PEF. When TCNQ doping is 20 mg and catalyst dosage is 50 mg, the catalytic effect is the best, and the degradation rate reaches 91.6%, $k = 0.0111 \text{ min}^{-1}$, which is four times that of g-C₃N₄. Repeated experiments found that the cyclic stability of the g-C₃N₄/TCNQ composite was good. The XRD images were almost unchanged after five reactions. The radical capture experiments revealed that $\cdot\text{O}_2^-$ was the main active species in the g-C₃N₄/TCNQ catalytic system, and h^+ also played a role in PEF degradation. And the possible mechanism for PEF degradation was speculated.

Keywords: TCNQ; graphite phase carbon nitride; pefloxacin; photocatalysis



Citation: Li, Q.; Wen, N.; Zhang, W.; Yu, L.; Shen, J.; Li, S.; Lv, Y. Preparation of g-C₃N₄/TCNQ Composite and Photocatalytic Degradation of Pefloxacin. *Micromachines* **2023**, *14*, 941. <https://doi.org/10.3390/mi14050941>

Academic Editor: Xuming Zhang

Received: 23 March 2023

Revised: 18 April 2023

Accepted: 20 April 2023

Published: 26 April 2023



Copyright: © 2023 by the authors. Licensee MDPI, Basel, Switzerland. This article is an open access article distributed under the terms and conditions of the Creative Commons Attribution (CC BY) license (<https://creativecommons.org/licenses/by/4.0/>).

1. Introduction

Antibiotics are a class of secondary metabolites produced by microorganisms or higher animals and plants in life with anti-pathogen or other activities [1,2]. Antibiotics enter the ecological environment because of their high-water solubility, lack of degradability, and other characteristics; they accumulate in the environment, and seriously destroy the balance of the ecological system [3,4]. Pharmaceutical wastewater in China has a large output and a wide distribution range every year, among which antibiotic wastewater accounts for the central part. Common antibiotics include quinolones, tetracycline, etc. [5]. Quinolone antibiotics are widely used, and their migration and transformation in the environment have received significant attention. According to the differences in antibacterial properties, the third-generation drugs represented by Pefloxacin (PEF), Norfloxacin (NOF), ciprofloxacin (CIP), and Levofloxacin (LEVX) are the most commonly used [6,7]. Quinolones (4-Quinolones), also known as pyridyl or pyridyl acids, are synthetic antibacterial drugs containing the basic structure of 4-quinolone. As broad-spectrum antibacterial drugs, quinolone antibiotics are used to treat infectious diseases in humans and animals due to their strong sterilization ability, good absorption by the body, and common adverse reactions. In recent years, the abuse of antibiotics has been severe [8–10]. Such drugs cannot be wholly metabolized after ingestion by organisms, and widely exist in pharmaceutical industry wastewater, medical wastewater, animal husbandry wastewater [11,12], and even surface water.

The semiconductor material g-C₃N₄ has excellent properties, such as high chemical and thermal stability, a flexible electronic structure, and a moderate band gap (2.7 eV). Due to its good biocompatibility and other characteristics, g-C₃N₄ has attracted significant attention in the industry and is widely used in photocatalysis [13,14], electrochemical sensing [15], bioimaging [16], drug delivery [17], and environmental monitoring, etc. [18–20].

Briefly speaking, photocatalytic technology refers to converting light energy into chemical energy by semiconductor materials under ultraviolet and visible light radiation, and the quick degradation or mineralization of pollutants. Organic pollutants harm the natural environment and can rapidly decompose into tiny, harmless molecular substances. The photocatalytic efficiency of pure $g\text{-C}_3\text{N}_4$ is often limited due to its high exciton binding energy, insufficient solar absorption, low surface area, and the tendency of photogenerated electron/hole pairs to rapidly complex [21,22]. Therefore, the modification of $g\text{-C}_3\text{N}_4$ is significant.

Wu et al. [23] showed that carbon dot-modified hollow porous $g\text{-C}_3\text{N}_4$ nanospheres have excellent photocatalytic degradation of naproxen under natural sunlight irradiation due to the excellent upconversion properties of carbon dots that can absorb and convert low-energy photons. Xiao et al. [24] developed a simple and cost-effective strategy to anchor copper single atoms to tubular $g\text{-C}_3\text{N}_4$ by inserting sodium chlorophyll copper into supramolecular precursors and subjecting them to heat treatment. The Cu atoms can be coordinated with three in-plane N atoms or four N atoms residing between two adjacent $g\text{-C}_3\text{N}_4$ layers to establish Cu-N_x charge transport channels, thus significantly facilitating the transfer of photogenerated carriers between the in-plane and interlayer. Ding et al. [25] showed that the rate of photocatalytic degradation of 2-chlorodibenzo-p-dioxin by $g\text{-C}_3\text{N}_4$ modified with palladium nanoparticles was 3.7 times higher than that of $g\text{-C}_3\text{N}_4$. This is because the Schottky barrier appears between Pd nanoparticles and $g\text{-C}_3\text{N}_4$, which expands the light absorption of $g\text{-C}_3\text{N}_4$ and hinders the complexation of photogenerated electron-hole pairs.

Research has shown that 7,7,8,8-tetracyano-p-phenylidiquinone methane (TCNQ) is an excellent organic electron acceptor, and it can form relatively stable charge transfer complexes with many transition metals, alkali metals, and other materials with electron donors [26]. These metal-organic complexes have good electrical, magnetic, and optical properties [27,28]. There has been much research on the compounds involved in the formation of TCNQ. One is the synthesis and characteristics of "organometallic" charge transfer salts formed by TCNQ and other organic compounds. Another is the synthesis and properties of organometallic compounds formed by TCNQ and metal ions [29,30].

Xie's group [31] successfully synthesized $\text{AgI} @ \text{TCNQ}$ composites for the photocatalytic degradation of methylene blue (MB) and found that the degradation rate of the composites was 1.8 times higher than that of AgI.

This paper synthesized a $g\text{-C}_3\text{N}_4/\text{TCNQ}$ composite, studied its photocatalytic performance, and applied it to the degradation of quinolone antibiotic PEF. This paper discusses the catalytic effect of different doping amounts and catalyst amounts and expounds on the active species, potential degradation mechanism, and cycle stability of $g\text{-C}_3\text{N}_4/\text{TCNQ}$ composite samples. It provides an advanced and green method for degrading antibiotics in wastewater, which is of great significance for improving the environment polluted by antibiotic wastewater.

2. Materials and Methods

2.1. Reagents and Instruments

The 7,7,8,8-Tetracyano-p-benzoquinone methane (TCNQ) was purchased from Aladdin Co., LTD. (Beijing, China), the melamine was purchased from Aladdin Industries (Beijing, China), the Pefloxacin (PEF) was purchased from Shanghai Jining Industrial Co., LTD. (Shanghai, China) the anhydrous ethanol was purchased from Tianjin Kaitong Chemical Reagent Co., LTD. (Tianjin, China), and the acetone was purchased from Tianjin Kaitong Chemical Reagent Co., LTD. (Tianjin, China).

Muffle Furnace (KSY-6D-16), Shenyang Energy-saving Electric Furnace Factory; Ultraviolet Spectrophotometer (UV-2550), Shimadzu Company, Guangzhou, China; X-ray diffractometer (3DMAX-IIIC), Nippon Shinosu Co., LTD., Kyoto, Japan; Fourier Transform Infrared Spectrometer (NEXUS-670), Thermo Fisher Scientific, New York, NY, USA.

2.2. Synthesis of $g\text{-C}_3\text{N}_4$

Synthesis of $g\text{-C}_3\text{N}_4$: The preparation of $g\text{-C}_3\text{N}_4$ was carried out by a thermal condensation method using melamine as a precursor. After being thoroughly ground down, 4 g melamine was put into the crucible, with a cover loosely on it. Then it was placed in a Muffle furnace. Under atmospheric conditions, the heating rate was controlled at $20\text{ }^\circ\text{C}/\text{min}$, and the temperature was heated to $550\text{ }^\circ\text{C}$ for 4 h. When the temperature cooled naturally to room temperature, it was removed from the Muffle furnace to obtain the light-yellow solid $g\text{-C}_3\text{N}_4$, which was ground into a powder for later use.

2.3. Preparation of $g\text{-C}_3\text{N}_4$ Copolymerized by TCNQ

Preparation of TCNQ doped $g\text{-C}_3\text{N}_4$: 4 g melamine and a certain amount of TCNQ were mixed up and evenly ground down, and then collected in the crucible, with a cover loosely on it. Then it was placed in a Muffle furnace. Under atmospheric conditions, the heating rate was controlled at $20\text{ }^\circ\text{C}/\text{min}$. It heated the temperature to $550\text{ }^\circ\text{C}$ for four h. After cooling to room temperature, the obtained $g\text{-C}_3\text{N}_4/\text{TCNQ-X}$ samples were taken out of the Muffle furnace and ground into a powder for later use, where x represented the added amount of TCNQ (x = 10 mg, 20 mg, 30 mg).

2.4. Photocatalytic Degradation of Pefloxacin in $g\text{-C}_3\text{N}_4/\text{TCNQ}$ Composites

A 50 mg $g\text{-C}_3\text{N}_4/\text{TCNQ}$ complex with different doping ratios was accurately weighed and dispersed in a 50 mL 10 mg/L PEF solution. The samples were dispersed under ultrasonic waves for 30 min to achieve the dispersion uniform and were placed in a dark environment for 30 min and magnetic stirring was used to achieve an adsorption–desorption equilibrium. Then, the xenon lamp (300 W) was set up to simulate the photocatalytic degradation experiment. Every 30 min, about 5 mL of the reaction liquid was taken for centrifuging twice. The absorbance of the supernatant was measured at 276 nm using an ultraviolet-visible spectrophotometer. The water circulation temperature had to be kept at about $20\text{ }^\circ\text{C}$ to avoid the influence of temperature on the experiment.

3. Results and Discussion

3.1. XRD Analysis

An X-ray diffractometer can be used to determine the crystal structure diagram. Figure 1 shows the XRD patterns of the $g\text{-C}_3\text{N}_4$ and $g\text{-C}_3\text{N}_4/\text{TCNQ}$ samples. It can be seen from the figure that distinct diffraction peaks appear at 13.1° and 27.4° , where the peak at 27.4° is the (002) peak of $g\text{-C}_3\text{N}_4$, reflecting the interlayer stacking structure of the aromatic triazine ring with an interlayer distance of $d = 0.326\text{ nm}$; the peak at 13.1° corresponds to the (100) peak of $g\text{-C}_3\text{N}_4$ s (100) peak, reflecting the in-plane structure of the triazine unit with an in-plane distance of $d = 0.676\text{ nm}$. The characteristic peak of the $g\text{-C}_3\text{N}_4$ material standard card (JCPDS-87-1526) is consistent [32]. The characteristic peaks of $g\text{-C}_3\text{N}_4$ did not shift significantly with the doping of TCNQ, which means that the $g\text{-C}_3\text{N}_4/\text{TCNQ}$ samples can maintain the graphene-like in-plane and interlayer characteristics of $g\text{-C}_3\text{N}_4$, indicating that the graphene-like structure of $g\text{-C}_3\text{N}_4$ was prepared by simple thermal copolymerization.

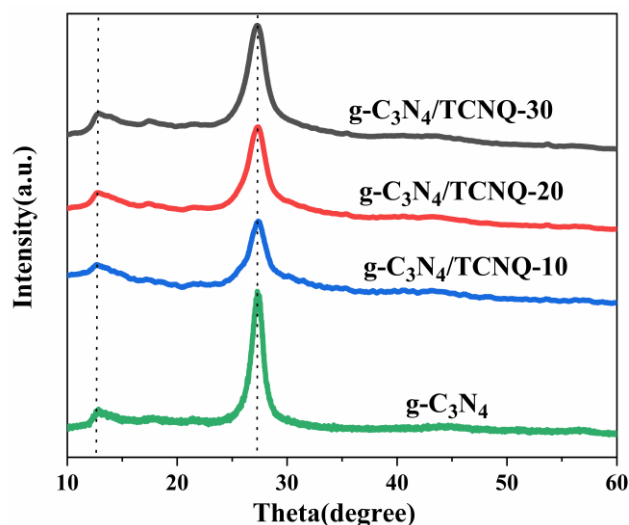


Figure 1. XRD patterns of $g\text{-C}_3\text{N}_4$ and $g\text{-C}_3\text{N}_4/\text{TCNQ}$.

3.2. FT-IR Analysis

Infrared spectroscopy is used to analyze the functional groups of the sample and further possible chemical structures. Figure 2 shows the FT-IR images of $g\text{-C}_3\text{N}_4$ and $g\text{-C}_3\text{N}_4/\text{TCNQ}$ samples. It can be seen from the figure that the characteristic spectra of all samples are similar. The absorption band located in the $1200\text{--}1700\text{ cm}^{-1}$ region is the characteristic resonance peak of the aromatic C-N heterocyclic repeating unit. In this range, peaks at 1240 , 1318 , and 1573 cm^{-1} correspond to C-NH-C, C-N and C=N keys in $g\text{-C}_3\text{N}_4$, respectively [33,34]. The absorption peak at 810 cm^{-1} corresponds to the structure of the 3-s-triazine ring (C_3N_3) [35]. In addition, the peak in the range of $3000\text{--}3500\text{ cm}^{-1}$ is an N-H bond [36]. The FT-IR results showed that TCNQ copolymerization did not change the chemical structure of $g\text{-C}_3\text{N}_4$. Because the doping amount is too low, no other response can be detected in $g\text{-C}_3\text{N}_4$ after TCNQ doping.

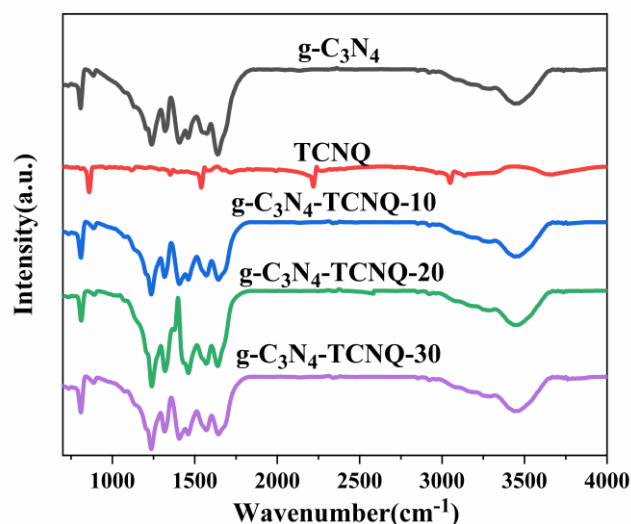


Figure 2. FT-IR images of $g\text{-C}_3\text{N}_4$ and $g\text{-C}_3\text{N}_4/\text{TCNQ}$ samples.

3.3. SEM Analysis

A scanning electron microscope (SEM) was used to observe the surface morphology of the samples. Figure 3 shows the SEM of the $g\text{-C}_3\text{N}_4$ and $g\text{-C}_3\text{N}_4/\text{TCNQ-20}$ samples. The figure shows that $g\text{-C}_3\text{N}_4$ has a large size sheet structure, and the size and thickness of $g\text{-C}_3\text{N}_4/\text{TCNQ}$ flake structures decreased, indicating that the copolymerization of TCNQ can significantly change the surface morphology of $g\text{-C}_3\text{N}_4$.

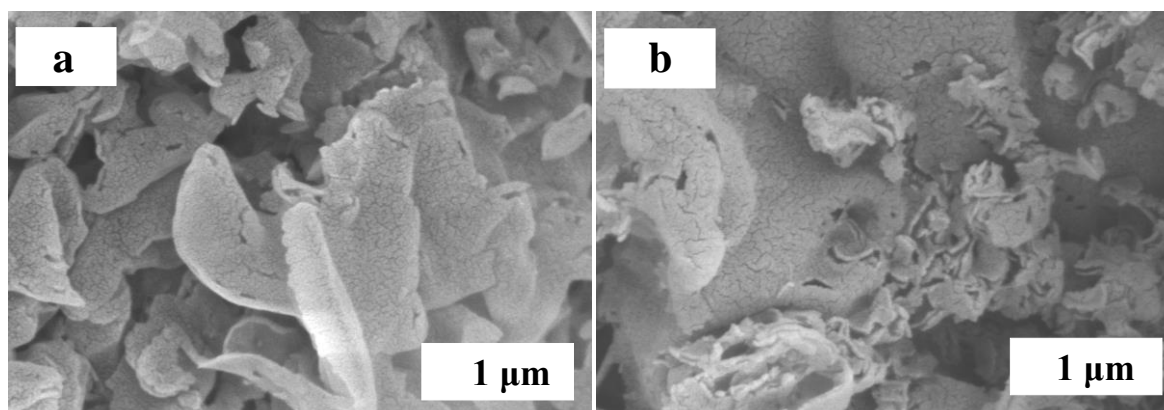


Figure 3. SEM images of (a) $g\text{-C}_3\text{N}_4$ and (b) $g\text{-C}_3\text{N}_4/\text{TCNQ-20}$.

3.4. TEM Analysis

Transmission electron microscopy (TEM) is used to observe the samples' further morphology and structural characteristics. Figure 4 shows the TEM images of $g\text{-C}_3\text{N}_4$ and $g\text{-C}_3\text{N}_4/\text{TCNQ-20}$, from which it can be observed that the samples are all two-dimensional nanomaterials. The original $g\text{-C}_3\text{N}_4$ two-dimensional sheet nanosheet has a large size, smooth surface, and integrity. With the addition of TCNQ doping, the $g\text{-C}_3\text{N}_4$ nanosheet size reduces and more pore structures emerge on the surface, indicating that the process of TCNQ copolymerization can lead to the fragmentation of nanosheets and thus produce pores on the surface of $g\text{-C}_3\text{N}_4$. This result is consistent with the results of the XRD analysis.

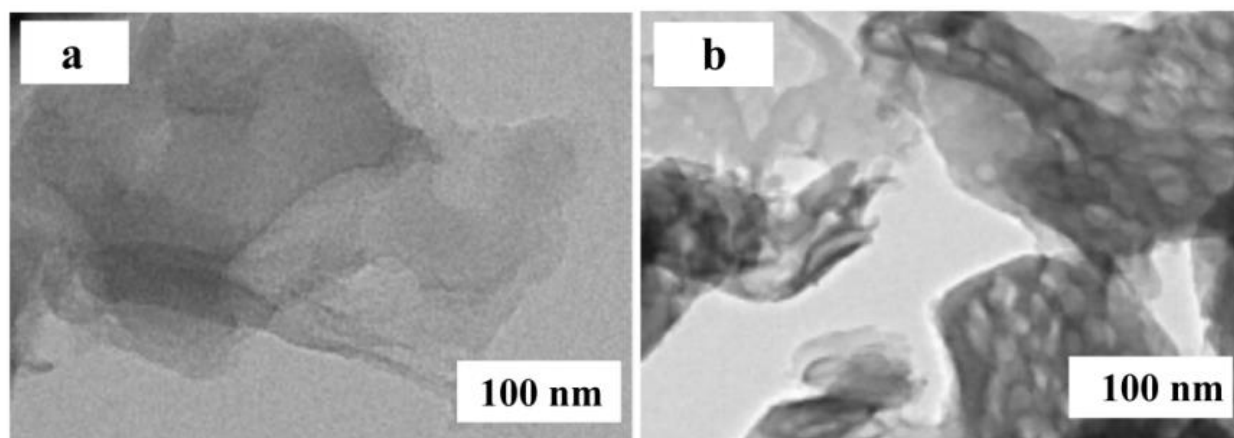


Figure 4. TEM images of (a) $g\text{-C}_3\text{N}_4$ and (b) $g\text{-C}_3\text{N}_4/\text{TCNQ-20}$.

3.5. DRS Analysis

UV-vis diffuse reflectance spectroscopy (DRS) was used to study the light absorption of prepared samples. Figure 5 shows the DRS diagram of the $g\text{-C}_3\text{N}_4$ and $g\text{-C}_3\text{N}_4/\text{TCNQ}$ samples. It can be seen from the figure that the absorption threshold of $g\text{-C}_3\text{N}_4$ samples occurs at 462 nm, and the corresponding bandgap width is 2.68 eV, which is consistent with the reported bandgap width of 2.7 eV [37]. The absorption thresholds of $g\text{-C}_3\text{N}_4/\text{TCNQ-10}$, $g\text{-C}_3\text{N}_4/\text{TCNQ-20}$, and $g\text{-C}_3\text{N}_4/\text{TCNQ-30}$ are 478 nm, 497 nm, and 491 nm, respectively, and the corresponding bandgap widths are 2.59 eV, 2.49 eV, and 2.52 eV, respectively. The corresponding band gap width also decreases. The absorption threshold of the sample is red-shifted, which may be caused by the nitrogen defect. The absence of an amino group will generate excess electrons in $g\text{-C}_3\text{N}_4$, making the carbon initially connected to $g\text{-C}_3\text{N}_4$ become C^{3+} and enter the conduction band, thus reducing the band gap width [38]. This indicates that TCNQ copolymerization can effectively narrow the band gap, increase the absorption of the visible light region, and increase the $g\text{-C}_3\text{N}_4/\text{TCNQ}$ samples' photoexcitation effectiveness and their photocatalytic activity, to a certain extent.

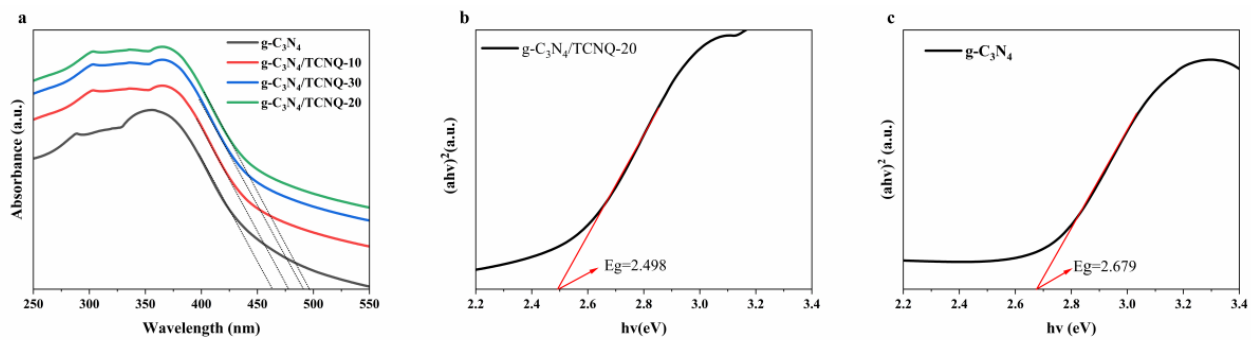


Figure 5. (a) UV-vis diffuse reflectance spectra, (b) forbidden band widths of g-C₃N₄/TCNQ composite samples and (c) forbidden band widths of g-C₃N₄ sample.

3.6. PL Analysis

The recombination of photogenerated electron–hole pairs generates fluorescence (PL) spectra, so measuring the intensity of PL spectra can help us better understand the photo-generated carriers' transmission and the recombination process in semiconductors. Figure 6 shows the photoluminescence spectra of g-C₃N₄ and g-C₃N₄/TCNQ samples. It can be seen from the figure that in the visible light wave region, all samples can generate fluorescent signals, indicating that electron–hole pairs can be generated when the material absorbs photons. This electron–hole pair is an essential step in inducing photoluminescence. With the increase of TCNQ doping, the intensity of the luminescence signal decreases gradually, and a photogenerated charge carrier recombination is prevented, which indicates that TCNQ doping can reduce the recombination rate of a photogenerated electron–hole and improve the separation efficiency. In general, the intensity of the fluorescence of the sample reflects the probability of a recombination of the generated electron–hole pair during the occurrence of a photocatalytic reaction. The higher the separation efficiency of the photogenerated electron–hole pair, the lower the recombination rate of the corresponding photogenerated charge carrier, the more conducive it is to the reaction of the electron–hole with the organic compound, and the higher the activity of the photocatalyst may be [39,40]. Moreover, when the doping amount of TCNQ increases, the PL peak position also shifts, consistent with the narrowness of the energy gap and the absorption redshift in the DRS spectrum.

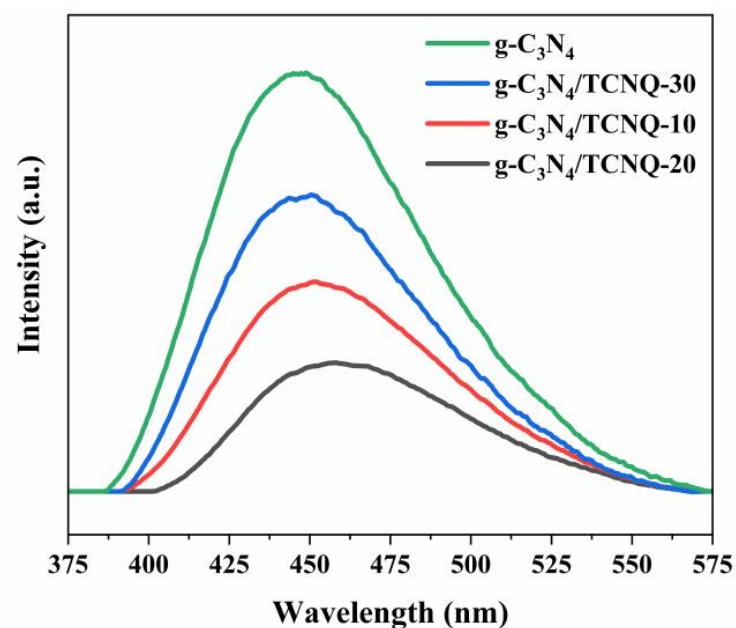


Figure 6. PL plots of the g-C₃N₄/TCNQ composite samples.

3.7. Photocurrent Test

The photocatalyst's instantaneous photocurrent was measured using a standard three-electrode system with a prepared catalytic film as the working electrode, a platinum plate as the reactive electrode, mercuric chloride as the reference electrode, and 0.1 M sodium sulfate as the electrolyte. The photoelectric properties of the prepared photocatalytic materials were obtained by measuring the photocurrent under visible light. The transient photocurrent responses (I-T) $g\text{-C}_3\text{N}_4$ and $g\text{-C}_3\text{N}_4/\text{TCNQ}$ prepared composite samples were measured. Figure 7 shows the I-T diagram of the two samples, from which it is apparent that when the light source is turned on, the current of both samples reaches the peak. When the light source is turned off, the photogenerated current decreases rapidly, indicating that the photogenerated electron holes in the material cause the current generation. The photogenerated current intensity of $g\text{-C}_3\text{N}_4/\text{TCNQ}$ is much stronger than that of $g\text{-C}_3\text{N}_4$, indicating that TCNQ copolymer doping is beneficial to separate photogenerated electrons and holes, and can generate more charge carriers, which is conducive to the improvement of photocatalytic activity [41].

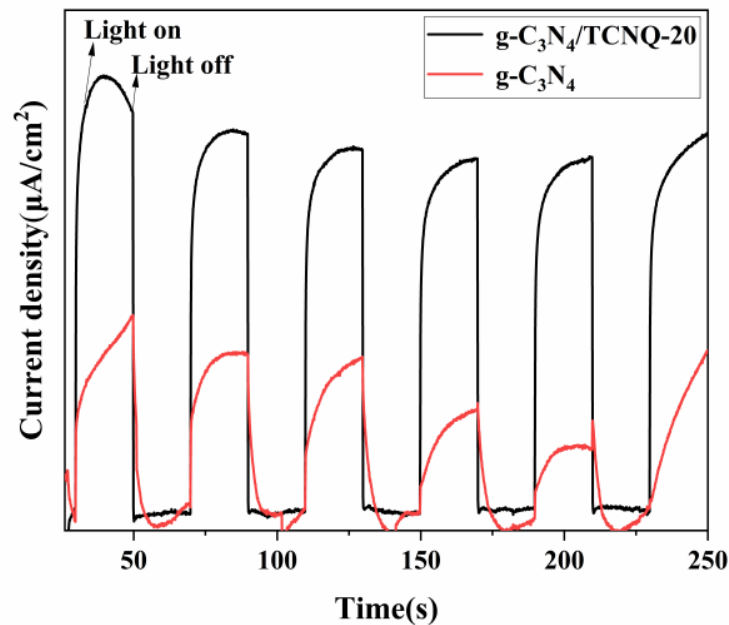


Figure 7. Transient photocurrent responses of $g\text{-C}_3\text{N}_4$ and $g\text{-C}_3\text{N}_4/\text{TCNQ}$ composites.

3.8. UV Absorption Spectroscopy

UV absorption spectra of PEF degradation by $g\text{-C}_3\text{N}_4/\text{TCNQ}$ composites showed that (Figure 8) the positions of the absorption peaks of the initial sample and the full-wavelength scan of the sample in the dark reaction stage remained the same. Only the intensity was slightly reduced, indicating that the adsorption process does not change the original state of the substance but only absorbs the pollutant molecules to the surface of the photocatalyst. After the adsorption equilibrium, visible light was added. The position of the original strong absorption peak changed with the increase in time. The peak intensity gradually decreased, and the peak intensity still decreased in the case of almost no adsorption. This indicates that the photocatalytic process destroyed the structure of antibiotics and generated other substances. The absorption of PEF at 272 nm decreased with the increase in light time, and it can also be seen that the maximum wavelength of absorption increased with the increase in light time. The absorption of PEF at 272 nm decreased with increasing light time, and it was also observed that the maximum wavelength of absorption decreased with increasing light time and showed a significant blue shift.

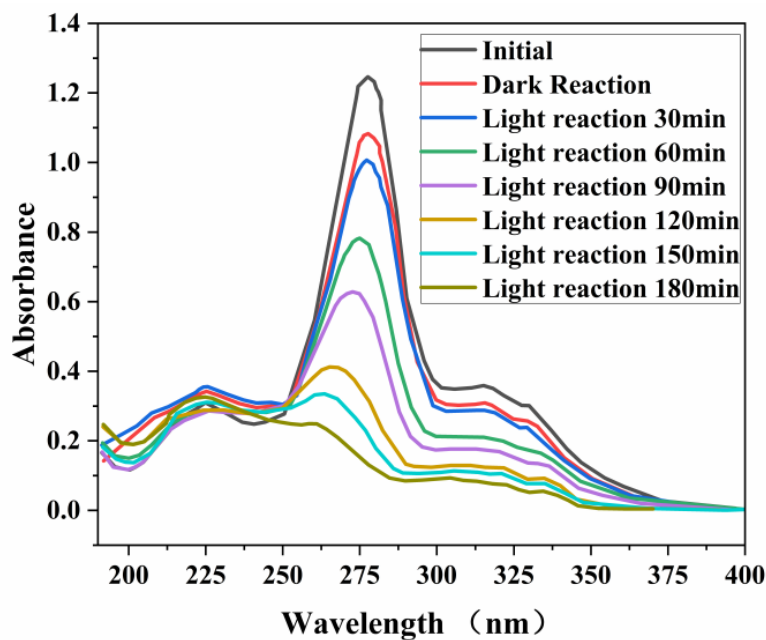


Figure 8. UV absorption spectra of PEF degradation by g-C₃N₄/TCNQ composites.

3.9. Influence of Different Drugs on Catalytic Effect

Figure 9a shows that: the g-C₃N₄/TCNQ-20 complex was taken and dispersed in PEF, ENR, and CIP drug solutions, and the samples were dispersed under ultrasonic waves for 30 min, and then dispersed uniformly in a dark environment with magnetic stirring for 30 min, called the dark reaction, and the dark reaction was finished and the light reaction was set to 0 points at the beginning.

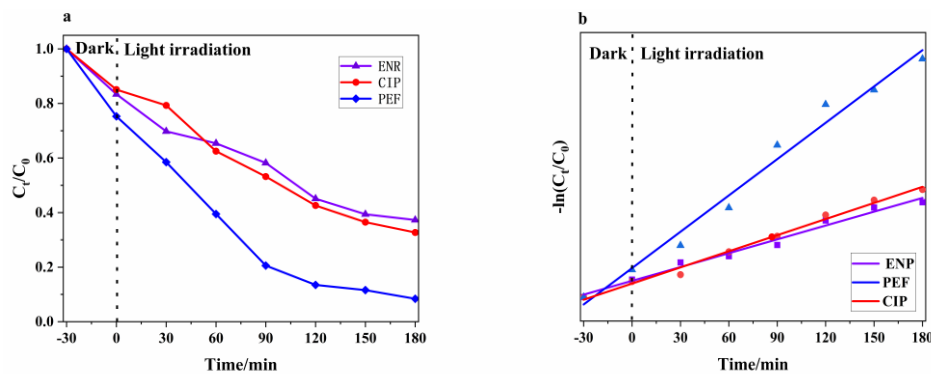


Figure 9. (a) Catalytic degradation of the different drug pairs by the g-C₃N₄/TCNQ composite (b) The kinetic curves of the first-order reaction for the different photocatalysts.

After 180 min of photocatalytic reaction, $D_{PEF} = 91.6\%$, $D_{ENR} = 62.7\%$ and $D_{CIP} = 67.3\%$. The experimental results showed that compared with ENR and CIP, the sample has the highest degradation rate of PEF and the best catalytic activity. This paper discusses the photocatalytic degradation kinetics of PEF, ENR, and CIP and adopts the first-order kinetic method to fit them [42]. The expression is: $\ln(C_0/C_t) = kt$, where C_0 and C_t are the concentrations of PEF, ENR, and CIP at time 0 and t, and k is the first-order velocity constant. Figure 9b shows an excellent linear relationship between $\ln(C_0/C_t)$ and the photocatalytic reaction time t for each drug.

3.10. Influence of Different Copolymer Doping Amounts on the Catalytic Effect of PEF

As can be seen from Figure 10, the dark reaction was performed for 30 min first, and g-C₃N₄ had a deficient photocatalytic activity with a $D_{PEF} = 36.8\%$ as the time increased.

While $g\text{-C}_3\text{N}_4$ can effectively absorb visible light, the $e^- \text{-} h^+$ pair's recombination rate is very high, inhibiting its photocatalytic activity. The D_{PEF} of $g\text{-C}_3\text{N}_4/\text{TCNQ-10}$ is 84.8%, the D_{PEF} of $g\text{-C}_3\text{N}_4/\text{TCNQ-20}$ is 91.6%, and the D_{PEF} of $g\text{-C}_3\text{N}_4/\text{TCNQ-30}$ is 73.4% after doping different qualities of TCNQ. The results showed that adding TCNQ could effectively inhibit the recombination of h^+ and e^- , enhancing the photocatalytic activity of $g\text{-C}_3\text{N}_4/\text{TCNQ}$. In the $g\text{-C}_3\text{N}_4/\text{TCNQ-20}$ sample, the degradation rate of PEF can reach 91.6%, and the catalytic activity is the best.

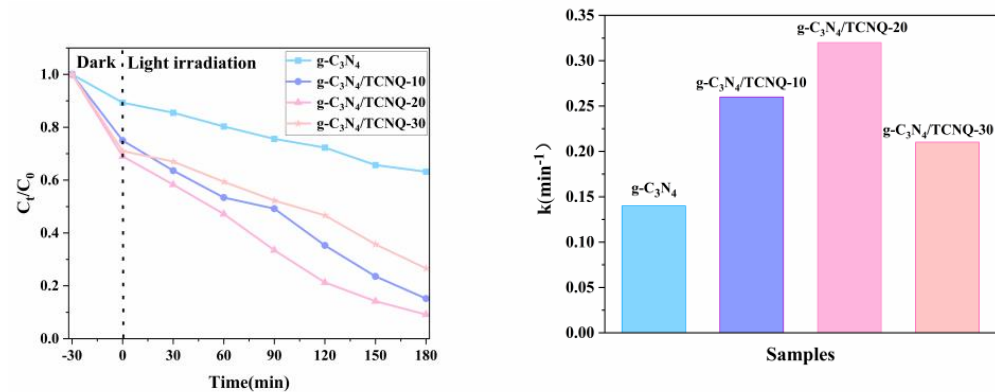


Figure 10. Photocatalytic effect of $g\text{-C}_3\text{N}_4/\text{TCNQ}$ samples with different TCNQ doping ratios.

3.11. Influence of Catalyst Dosage on Catalytic Effect of PEF

Figure 11 shows the photocatalytic effect diagram of samples with different masses of $g\text{-C}_3\text{N}_4/\text{TCNQ-20}$ at a PEF of 10 mg/L. 10 mg $D_{\text{PEF}} = 44.16\%$, 20 mg $D_{\text{PEF}} = 64.31\%$, 30 mg $D_{\text{PEF}} = 80.69\%$, 40 mg $D_{\text{PEF}} = 85.73\%$, 50 mg $D_{\text{PEF}} = 90.07\%$, 60 mg $D_{\text{PEF}} = 91.32\%$. As can be seen from the figure, the best addition was 60 mg and the worst addition was 10 mg as the amount of $g\text{-C}_3\text{N}_4/\text{TCNQ-20}$ samples added decreased. This change is because the more significant the amount of $g\text{-C}_3\text{N}_4/\text{TCNQ-20}$ that is used under the same illumination, the more photogenerated electron holes are generated. That is, more active substances are generated. Therefore, with the increase in the dosage, its degradation effect will also be enhanced. However, when the amount of catalyst is large, the increased value of the catalytic reaction speed is low. When the amount of catalyst is increased from 50 mg to 60 mg, the catalytic reaction speed is not significantly improved. Because the amount of $g\text{-C}_3\text{N}_4/\text{TCNQ-20}$ is too large, it will obviously scatter and reflect visible light, reduce the absorption of visible light, and then reduce the utilization rate of visible light, resulting in a decrease in the ability of photocatalytic degradation. Therefore, 50 mg of $g\text{-C}_3\text{N}_4/\text{TCNQ-20}$ is the optimal dosage.

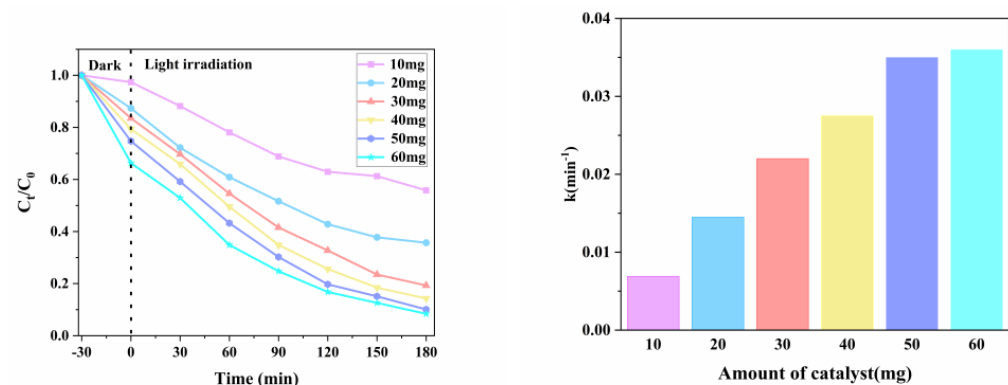


Figure 11. Influence of catalyst usage on the catalytic effect of PEF.

3.12. Kinetic Evaluation of the Photocatalytic Process of Catalyst PEF Degradation

Figure 12 shows the photocatalytic degradation kinetics of PEF, which was fitted using the first-order kinetic method. The composite sample was exposed to a dark reaction in PEF

for 30 min to reach the adsorption–desorption equilibrium. The end time of the reaction in the dark and the start time of the reaction in the light was set to zero, and the kinetics of the photocatalytic reaction were studied. The conclusion is that the relationship between $\ln(C_0/C_t)$ and the photocatalytic reaction time t is linear for each sample.

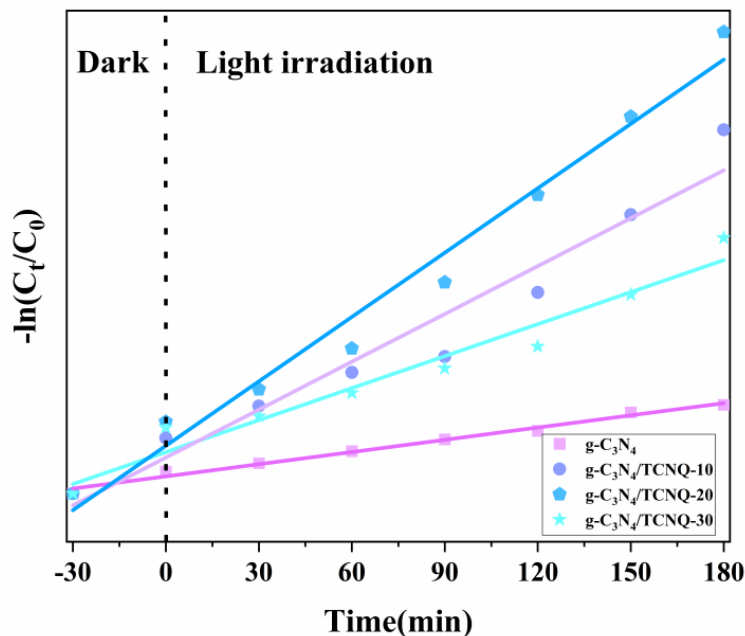


Figure 12. First-order reaction constants of $g-C_3N_4/TCNQ$ -mediated degradation of PEF.

As shown in Table 1, the k value of $g-C_3N_4/TCNQ-20$ is greater, $k = 0.0111 \text{ min}^{-1}$, and has the highest degree of PEF degradation, which is about four times that of $g-C_3N_4$. The R^2 of each $g-C_3N_4/TCNQ$ composite sample is greater than 0.9, thus concluding that each sample satisfies the match between the D_{PEF} and the first-order reaction kinetic equation.

Table 1. Linear fitting data of photocatalytic degradation kinetics of PEF in $g-C_3N_4/TCNQ$ composite samples.

| Sample Name | Regression Equation | k | R^2 |
|--------------------|------------------------|--------|--------|
| $g-C_3N_4$ | $y = 0.0021x + 0.0885$ | 0.0021 | 0.9888 |
| $g-C_3N_4/TCNQ-10$ | $y = 0.0083x + 0.1862$ | 0.0083 | 0.9523 |
| $g-C_3N_4/TCNQ-20$ | $y = 0.0111x + 0.2471$ | 0.0111 | 0.9800 |
| $g-C_3N_4/TCNQ-30$ | $y = 0.0055x + 0.2143$ | 0.0055 | 0.9578 |

3.13. Analysis of Experimental Results for Reuse of PEF Degradation

Figure 13 shows the catalyst stable cycle diagram, where the used $g-C_3N_4/TCNQ-20$ photocatalyst was collected by centrifugation and washed three times with water and alcohol. After drying in an oven at $60 \text{ }^\circ\text{C}$, an equal amount of dry powder was used as a photocatalyst for the next cycle run. After repeating the experiment four times, the first degradation effect was the best, and then the degradation rate each time decreased. However, the change was insignificant, and the catalyst still had a high degradation rate of about 80%. The results show that the catalyst has good stability, renewable performance, and can be reused. Furthermore, the XRD spectra of the reused catalysts (Figure 14) showed no significant changes in their crystal properties, which indicated the comparative stability of the prepared catalysts. The results indicate that $g-C_3N_4/TCNQ$ is an efficient and stable visible-light-driven photocatalyst for the degradation of quinolones.

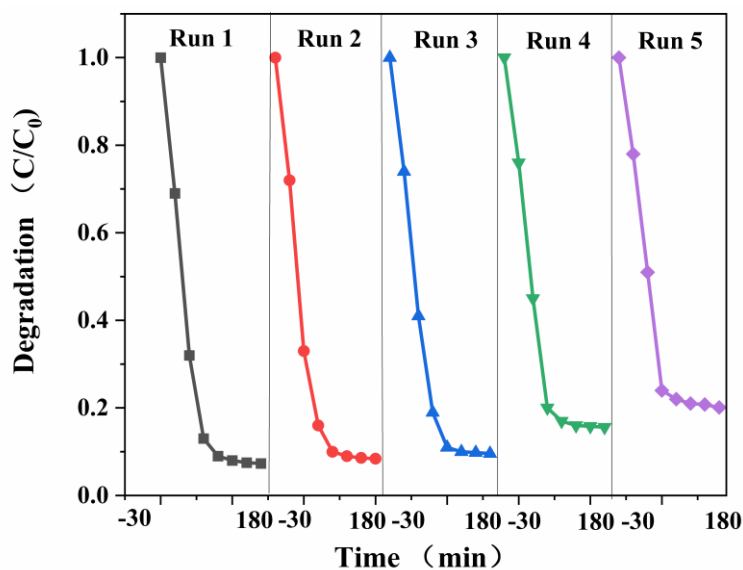


Figure 13. Reuse experiment of $g\text{-C}_3\text{N}_4/\text{TCNQ}$ composite material degrading PEF.

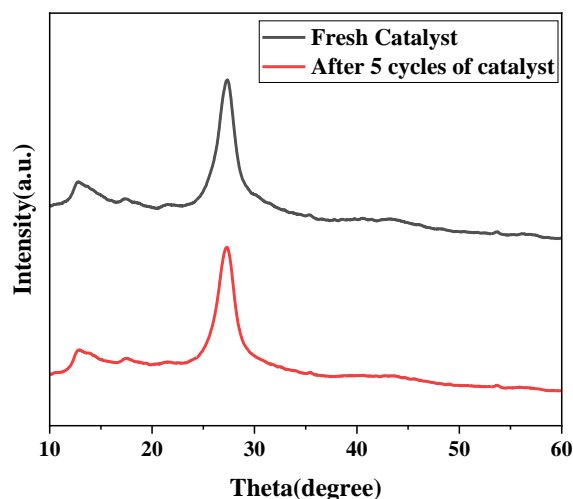


Figure 14. XRD patterns of $g\text{-C}_3\text{N}_4/\text{TCNQ}$ samples before and after reuse.

3.14. Analysis of Free Radical Capture Experimental Results of PEF Degradation by Catalyst

Free radical trapping experiments can analyze the main active components in photocatalysis, and the possible mechanism is discussed. In this study, three different trapping agents, 1,4-benzoquinone (BQ), tert-butyl alcohol (TBA), ethylenediamine tetraacetate sodium (EDTA-2Na), were used to capture superoxide radical ($\cdot\text{O}_2^-$), hydroxyl radical ($\cdot\text{OH}$), and hole (h^+), respectively. The experimental results are shown in Figure 15. It can be seen from the figure that when no capture agent is added, the degradation rate of PEF by $g\text{-C}_3\text{N}_4/\text{TCNQ}$ -20 can still reach 90.8%. When the capture agents BQ, TBA, and EDTA are added, the degradation rate drops to 26.8%, 85.2%, and 67.2%, respectively. When BQ was added to the system to remove superoxide radicals, the photocatalytic degradation rate was significantly inhibited, indicating that superoxide radicals were the main active substances. At the same time, adding EDTA can also reduce the speed of the photocatalytic reaction, indicating that h^+ also plays a vital role in the photocatalytic reaction. After the addition of TBA, the rate of its catalytic degradation did not decrease significantly compared with that without the addition of the capture agent, which indicated that the elimination of $\cdot\text{OH}$ did not significantly influence the photocatalytic reaction. Therefore, $\cdot\text{O}_2^-$ and h^+ are the main active species in the $g\text{-C}_3\text{N}_4/\text{TCNQ}$ catalytic system. Among them, $\cdot\text{O}_2^-$ is more critical for PEF degradation.

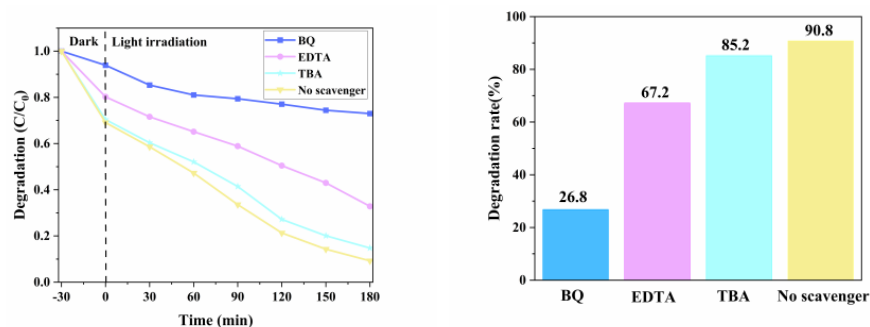


Figure 15. Effect of different radical capture agents on catalytic degradation.

3.15. Photocatalytic Mechanism Analysis

It can be seen from the above results that the photocatalytic activity of the g-C₃N₄/TCNQ composite sample is higher than that of the g-C₃N₄. On this basis, it is hypothesized how the g-C₃N₄/TCNQ composite sample photo-catalytically degrades PEF. Since the g-C₃N₄/TCNQ sample with a lower gap width than g-C₃N₄ is more likely to accept lower photon energy intensity, the electrons on VB (e⁻) jump into CB through the gap and form a photogenerated carrier hole (e⁻-h⁺). The photogenerated electrons on CB are transferred to VB on the material’s surface, e⁻ reacts with O₂ in solution to generate ·O²⁻, and ·O²⁻ reacts with PEF to generate intermediate substances and then generates small molecular substances. On the other hand, h⁺ on VB directly reacts with PEF, and then catalyzes PEF degradation to increase the composite sample’s capacity for photocatalysis. Figure 16 shows the possible mechanism for PEF degradation.

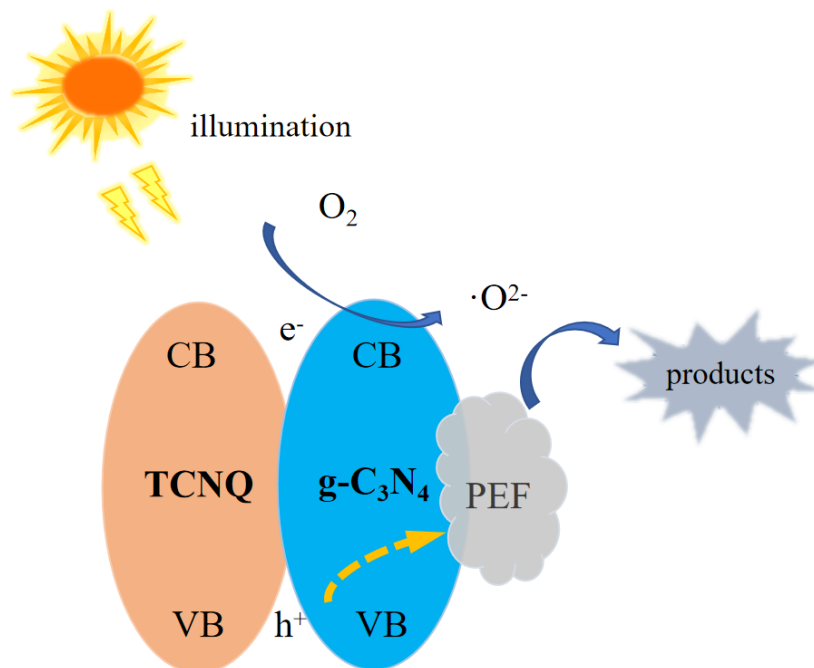


Figure 16. Possible degradation mechanism of PEF.

4. Conclusions

In this paper, a g-C₃N₄, g-C₃N₄/TCNQ complex was successfully prepared using the coprothermal method, and characterized by XRD, FT-IR, SEM, TEM, DRS, PL, and I-T. PEF was employed as a degradation product to assess the catalyst’s photocatalytic properties, and PEF was broken down under visible light (>550 nm) to examine the photocatalytic activity. When the doping amount of g-C₃N₄/TCNQ-20 was 50 mg, the D_{PEF} was 91.6%. All of the sample pairs of D_{PEF} conformed to the first-order kinetic equation when combined with the kinetic analysis of the photocatalytic reaction, four times more

than g-C₃N₄ alone. After five cycles, the photodegradation activity of the g-C₃N₄/TCNQ composite sample was still as high as 80%. The free radical capture experiments found that ·O²⁻ was the main active species of the g-C₃N₄/TCNQ catalytic system, h⁺ also plays a role in the degradation of PEF. This study provides an advanced and green method for the degradation of antibiotics in wastewater and provides a theoretical basis for improving the pollution of antibiotic wastewater.

Author Contributions: Q.L., N.W. and Y.L.: writing—original draft, writing—review and editing, methodology, formal analysis; J.S., L.Y. and W.Z.: writing—original draft, formal analysis, visualization, project administration; N.W. and S.L.: data analysis; and Y.L.: resources. All authors have read and agreed to the published version of the manuscript.

Funding: This research was funded by [the National Natural Science Foundation of China] grant number [21346006], and the APC was funded by [Yuguang Lv]. [Department of scientific research project in Heilongjiang province] grant number [LH2022B022], and the APC was funded by [Yuguang Lv]. [the Innovation and Entrepreneurship Project for College students in Heilongjiang Province] grant number [S202210222075], and the APC was funded by [Yuguang Lv].

Institutional Review Board Statement: Not applicable.

Informed Consent Statement: Not applicable.

Data Availability Statement: The data is unavailable due to privacy or ethical restrictions.

Conflicts of Interest: The authors declare no conflict of interest.

References

1. Cheng, X.; Yu, X.; Zhu, H. Research progress on antibiotic pollution and its treatment technology in water bodies. *Environ. Sci. Technol.* **2017**, *40*, 125–132.
2. Scott, G.I.; Porter, D.E.; Norman, R.S.; Scott, C.H.; Uyaguari-Diaz, M.I.; Maruya, K.A.; Weisberg, S.B.; Fulton, M.H.; Wirth, E.F.; Moore, J.; et al. Antibiotics as CECs: An overview of the hazards posed by antibiotics and antibiotic resistance. *Front. Mar. Sci.* **2016**, *3*, 24. [[CrossRef](#)]
3. Huijbers, P.M.; Flach, C.F.; Larsson, D.J. A conceptual framework for the environmental surveillance of antibiotics and antibiotic resistance. *Environ. Int.* **2019**, *130*, 104880. [[CrossRef](#)] [[PubMed](#)]
4. Surette, M.D.; Wright, G.D. Lessons from the environmental antibiotic Resistome. *Annu. Rev. Microbiol.* **2017**, *71*, 309–329. [[CrossRef](#)]
5. Kim, S.C.; Carlson, K. Occurrence of ionophore antibiotics in water and sediments of a mixed-landscape watershed. *Water Res.* **2006**, *40*, 2549–2560. [[CrossRef](#)]
6. Zhao, X.; Chu, Z.; Li, Y. Molecular design and photolysis path inference. *J. Chem. High. Educ.* **2018**, *39*, 2707–2718.
7. Pham, T.; Ziora, Z.M.; Blaskovich, M. Quinolone antibiotics. *Med. Chem. Commun.* **2019**, *10*, 1719–1739. [[CrossRef](#)]
8. Tang, K.; Zhao, H. Quinolone antibiotics: Resistance and therapy. *Infect. Drug Resist.* **2023**, *16*, 811–820. [[CrossRef](#)]
9. Bai, H.; Zhang, Q.; Zhou, X.; Chen, J.; Chen, Z.; Liu, Z.; Yan, J.; Wang, J. Removal of fluoroquinolone antibiotics by adsorption of dopamine-modified bio-char aerogel. *Korean J. Chem. Eng.* **2023**, *40*, 811–820. [[CrossRef](#)]
10. Zhang, Y.; Yan, X.J.; Sun, Y. Current situation of antibiotic abuse in China and its residues distribution in the environment. *Contemp. Chem. Ind.* **2019**, *48*, 2660–2662.
11. Ahmad, F.; Zhu, D.; Sun, J. Environmental fate of tetracycline antibiotics: Degradation pathway mechanisms, challenges, and perspectives. *Environ. Sci. Eur.* **2021**, *33*, 64. [[CrossRef](#)]
12. Mathur, P.; Sanyal, D.; Dey, P. The optimization of enzymatic oxidation of levofloxacin, a fluoroquinolone antibiotic for waste water treatment. *Biodegradation* **2021**, *32*, 467–485. [[CrossRef](#)] [[PubMed](#)]
13. Yang, W.; Ding, K.; Chen, G.; Wang, H.; Deng, X. Synergistic multisystem photocatalytic degradation of anionic and cationic dyes using graphitic phase carbon nitride. *Molecules* **2023**, *28*, 2796. [[CrossRef](#)] [[PubMed](#)]
14. Luo, J.; Du, X.; Ye, Q.; Fu, D. Review: Graphite phase carbon nitride photo-fenton catalyst and its photocatalytic degradation performance for organic wastewater. *Catal. Surv. Asia* **2022**, *26*, 294–310. [[CrossRef](#)]
15. Li, K.; Cui, J.; Yang, Q.; Wang, S.; Luo, R.; Argenis, R.G.; Wei, P.; Liu, L. A new sensor for the rapid electrochemical detection of ractopamine in meats with high sensitivity. *Food Chem.* **2022**, *405*, 134791. [[CrossRef](#)]
16. Zhan, Y.; Liu, Z.; Liu, Q.; Huang, D.; Wei, Y.; Hu, Y.; Lian, X.; Hu, C. A facile and one-pot synthesis of fluorescent graphitic carbon nitride quantum dots for bio-imaging applications. *New J. Chem.* **2017**, *41*, 3930–3938. [[CrossRef](#)]
17. Dong, J.; Zhao, Y.; Chen, H.; Liu, L.; Zhang, W.; Sun, B.; Yang, M.; Wang, Y.; Dong, L. Fabrication of PEGylated graphitic carbon nitride quantum dots as traceable, pH-sensitive drug delivery systems. *New J. Chem.* **2018**, *42*, 14263–14270. [[CrossRef](#)]
18. Wang, M.; Ma, F.; Wang, Z. Graphitic carbon nitride, a saturable absorber material for the visible waveband. *Photonics Res.* **2018**, *6*, 307–313. [[CrossRef](#)]

19. Ong, W.J.; Tan, L.L.; Ng, W.H. Graphitic carbon nitride (g-C₃N₄)-based photocatalysts for artificial photosynthesis and environmental remediation: Are we a step closer to achieving sustainability? *Chem. Rev.* **2016**, *116*, 7159–7329. [[CrossRef](#)]
20. Chen, L.C.; Song, J.B. Tailored graphitic carbon nitride nanostructures: Synthesis, modification, and sensing applications. *Adv. Funct. Mater.* **2017**, *27*, 1702695. [[CrossRef](#)]
21. Mamba, G.; Mishra, A.K. Graphitic carbon nitride (g-C₃N₄) nanocomposites: A new and exciting generation of visible light driven photocatalysts for environmental pollution remediation. *Appl. Catal. B Environ.* **2016**, *198*, 347–377. [[CrossRef](#)]
22. Cao, S.; Low, J.; Yu, J. Polymeric photocatalysts based on graphitic carbon nitride. *Adv. Mater.* **2015**, *27*, 2150–2176. [[CrossRef](#)] [[PubMed](#)]
23. Wu, Y.; Wang, F.; Jin, X.; Zheng, X.; Wang, Y.; Wei, D.; Zhang, Q.; Feng, Y.; Xie, Z.; Chen, P. Highly active metal-free carbon dots/g-C₃N₄ hollow porous nanospheres for solar-light-driven PPCPs remediation: Mechanism insights, kinetics and effects of natural water matrices. *Water Res.* **2020**, *172*, 115492. [[CrossRef](#)] [[PubMed](#)]
24. Xiao, X.; Gao, Y.; Zhang, L.; Zhang, J.; Zhang, Q.; Li, Q.; Bao, H.; Zhou, J.; Miao, S.; Chen, N. A promoted charge separation/transfer system from Cu single atoms and C₃N₄ layers for efficient photocatalysis. *Adv. Mater.* **2020**, *32*, 2003082. [[CrossRef](#)] [[PubMed](#)]
25. Ding, J.; Long, G.; Luo, Y.; Sun, R.; Chen, M.; Li, Y.; Zhou, Y.; Xu, X.; Zhao, W. Photocatalytic reductive dechlorination of 2-chlorodibenzo-p-dioxin by Pd modified g-C₃N₄ photocatalysts under UV-vis irradiation: Efficacy, kinetics and mechanism. *J. Hazard. Mater.* **2018**, *355*, 74–81. [[CrossRef](#)]
26. Üngör, Ö.; Phan, H.; Choi, E.S.; Roth, J.K.; Shatruk, M. Magnetism and electrical conductivity of molecular semiconductor, [Fe II (DMF) 4 (TCNQ) 2](TCNQ) 2, with fraction-ally charged TCNQ units. *J. Magn. Magn. Mater.* **2020**, *497*, 165984. [[CrossRef](#)]
27. Nafady, A.; Sabri, Y.M.; Kandjani, A.E.; Alsalmeh, A.M.; Bond, A.M.; Bhargava, S. Preferential synthesis of highly conducting TI(TCNQ) phase II nanorod networks via electrochemically driven TCNQ/TI(TCNQ) solid-solid phase transformation. *J. Solid State Electrochem.* **2016**, *20*, 3303–3314. [[CrossRef](#)]
28. Tamaya, H.; Torii, Y.; Ishikawa, T.; Nakano, H.; Iimori, T. Photophysics and inverted solvatochromism of 7,7,8,8-tetracyanoquinodimethane (TCNQ). *Chemphyschem A Eur. J. Chem. Phys. Phys. Chem.* **2019**, *20*, 2531–2538. [[CrossRef](#)]
29. Iwano, Y.; Kittaka, T.; Tabuchi, H. Study of amorphous carbon nitride films aiming at white light emitting devices. *Jpn. J. Appl. Phys.* **2008**, *47*, 7842–7844. [[CrossRef](#)]
30. Zhu, C.Z.; Du, D.; Lin, Y.H. Graphene-like 2D nanomaterial-based biointerfaces for biosensing applications. *Biosens. Bioelectron.* **2017**, *89*, 43–55. [[CrossRef](#)]
31. Xie, W.; Liu, L.; Cui, W.; An, W. Enhancement of photocatalytic activity under visible light irradiation via the AgI@TCNQ core-shell structure. *Materials* **2019**, *12*, 1679. [[CrossRef](#)] [[PubMed](#)]
32. Ye, C.; Li, J.X.; Li, Z.J. Enhanced driving force and charge separation efficiency of protonated g-C₃N₄ for photocatalytic O₂ Evolution. *ACS Catal.* **2015**, *5*, 6973–6979. [[CrossRef](#)]
33. Zhang, J.; Zhu, Z.; Tang, Y.; Mullen, K.; Feng, X. Titania nanosheet-mediated construction of a two-dimensional titania/cadmium sulfide heterostructure for high hydrogen evolution activity. *Adv. Mater.* **2014**, *26*, 734–738. [[CrossRef](#)] [[PubMed](#)]
34. She, X.; Liu, L.; Ji, H.; Mo, Z.; Li, Y.; Huang, L.; Du, D.; Xu, H.; Li, H. Template-free synthesis of 2D porous ultrathin nonmetal-doped g-C₃N₄ nanosheets with highly efficient photocatalytic H₂ evolution from water under visible light. *Appl. Catal. B* **2016**, *187*, 144–153. [[CrossRef](#)]
35. Wang, F.; Chen, P.; Feng, Y.; Xie, Z.; Liu, Y.; Su, Y.; Zhang, Q.; Wang, Y.; Yao, K.; Lv, W.; et al. Facile synthesis of N-doped carbon dots/g-C₃N₄ photocatalyst with enhanced visible-light photo-catalytic activity for the degradation of indomethacin. *Appl. Catal. B* **2017**, *207*, 103–113. [[CrossRef](#)]
36. Li, Y.; Shi, J. Hollow-structured mesoporous materials: Chemical synthesis, functionalization and applications. *Adv. Mater.* **2014**, *26*, 3176–3205. [[CrossRef](#)]
37. Wang, X.; Maeda, K.; Thomas, A. A metal-free polymeric photocatalyst for hydrogen production from water under visible light. *Nat. Mater.* **2009**, *8*, 76–80. [[CrossRef](#)]
38. Niu, P.; Yin, L.-C.; Yang, Y.-Q. Increasing the visible light absorption of graphitic carbon nitride (melon) photocatalysts by homogeneous self-modification with nitrogen vacancies. *Adv. Mater.* **2014**, *26*, 8046–8052. [[CrossRef](#)]
39. Zhang, X.; Peng, B.; Zhang, S.; Peng, T. Robust wide visible-light-responsive photoactivity for H₂ production over a polymer/polymer heterojunction photocatalyst: The significance of sacrificial reagent. *ACS Sustain. Chem. Eng.* **2015**, *3*, 1501–1509. [[CrossRef](#)]
40. Wu, J.; Li, B.-H.; Zhong, H.-R.; Qiu, S.-W.; Liang, Y.-W.; Zhuang, X.-Y.; Singh, A.; Kumar, A. Fluorescence sensing and photocatalytic properties of a 2D stable and bio-compatible Zn(II)-based polymer. *J. Mol. Struct.* **2018**, *1158*, 264–270. [[CrossRef](#)]
41. Li, Y.; Wu, S.; Huang, L.; Wang, J.; Xu, H.; Li, H. Synthesis of carbon-doped g-C₃N₄ composites with enhanced visible-light photocatalytic activity. *Mater. Lett.* **2014**, *137*, 281–284. [[CrossRef](#)]
42. Yan, Y.; Chang, T.; Wei, P.; Kang, S.Z.; Mu, J. Photocatalytic activity of nano-composites of ZnO and multi-walled carbon nanotubes for dye degradation. *J. Dispers. Sci. Technol.* **2009**, *30*, 198–203. [[CrossRef](#)]

Disclaimer/Publisher’s Note: The statements, opinions and data contained in all publications are solely those of the individual author(s) and contributor(s) and not of MDPI and/or the editor(s). MDPI and/or the editor(s) disclaim responsibility for any injury to people or property resulting from any ideas, methods, instructions or products referred to in the content.